Check for updates

Large piezoelectric response in ferroelectric/multiferroelectric metal oxyhalide MOX$_2$ (M = Ti, V and X = F, Cl and Br) monolayers†

Mohammad Noor-A-Alam [ID] * and Michael Nolan [ID] *

Flexible two-dimensional (2D) piezoelectric materials are promising for applications in wearable electromechanical nano-devices such as sensors, energy harvesters, and actuators. A large piezo-response is required for any practical applications. Based on first-principles calculations, we report that ferroelectric TiOX$_2$ and multiferroelectric VOX$_2$ (X = F, Cl, and Br) monolayers exhibit large in-plane stress (e_{11}) and strain (d_{11}) piezoelectric coefficients. For example, the in-plane piezo-response of TiOBr$_2$ (both e_{11} = 28.793 × 10^{-10} C m^{-1} and d_{11} = 37.758 pm V^{-1}) is about an order of magnitude larger than that of the widely studied 1H-MoS$_2$ monolayer, and also quite comparable to the giant piezoelectricity of group-IV monochalcogenide monolayers, *e.g.*, SnS. Moreover, the d_{11} of MOX$_2$ monolayers – ranging from 29.028 pm V^{-1} to 37.758 pm V^{-1} – are significantly higher than the d_{11} or d_{33} of commonly used 3D piezoelectrics such as w-AlN (d_{33} = 5.1 pm V^{-1}) and α-quartz (d_{11} = 2.3 pm V^{-1}). Such a large d_{11} of MOX$_2$ monolayers originates from low in-plane elastic constants with large e_{11} due to large Born effective charges (Z_{ij}) and atomic sensitivity $\left(\dfrac{du}{d\eta}\right)$ to an applied strain. Moreover, we show the possibility of opening a new way of controlling piezoelectricity by applying a magnetic field.

1 Introduction

Insulators or semiconductors that lack inversion symmetry exhibit a piezoelectric effect, which is an electromechanical coupling that allows energy conversion from mechanical to electrical, and *vice versa*. This effect is used in many important applications such actuators, sensors, and transducers.[1,2] Current trends in the miniaturization of devices require piezoelectricity at the nanoscale. Being at most a few atomic-layers thick, 2D piezoelectrics have potential for miniaturizing these electromechanical devices down to nanoscale. Moreover, compared with 3D piezoelectrics (*e.g.*, bulk crystals or thin-films), few layered (typically 1–3 layers) piezoelectric materials can generally exhibit larger deformation.[1,2] Importantly, nowadays these 2D materials can be grown with good crystalline quality. Hence, 2D piezoelectrics become promising for self-powered, flexible, and wearable nano-devices. These 2D piezoelectrics can also

find interesting applications in new types of electronics such as piezotronics[1] – where the electronic band gap is controlled by the electric potential stemming from piezoelectricity – and in piezo-photonics,[2] where light is coupled with the piezoelectrically induced charges. For example, it has been predicted that the performance of MoS$_2$-based solar cells can be enhanced by the coupling of semiconducting and piezoelectric properties.[3]

Quite often, reduction in materials dimension promotes unique properties. For example, bulk 2H-MoS$_2$ is a non-piezoelectric due to its centrosymmetry, whereas the monolayer (also odd numbered layers *e.g.*, trilayer) has no inversion symmetry – and exhibits piezoelectric properties.[4] In agreement with the theory,[4] in-plane piezoelectricity in a 1H-MoS$_2$ monolayer, which is comparable to the piezo-response of commercially used wurtzite nitrides, *e.g.*, the d_{33} of w-AlN (5.1 pm V^{-1}), has been confirmed by recent experiments.[5] However, generally speaking, a high piezo-response in these 2D materials is desired for any device-level applications. Therefore, enhancement of piezoelectricity and discovery of new 2D piezoelectrics have drawn significant research interest. Typically, 1H-type (D_{3h} symmetry)[6–9] (*e.g.*, d_{11} = 13.45 pm V^{-1} for 1H-CrTe$_2$[6] and Janus 1T-type[10–12] (*e.g.*, d_{22} = 4.12 pm V^{-1} for 1T-MoSSe)[10] 2D materials have been investigated for a large piezoelectric response. So far, piezoelectricity has been predicted in several families of non-ferroelectric 2D materials, like doped or chemi-

Tyndall National Institute, Lee Maltings, Dyke Parade, University College Cork, T12R5CP Cork, Ireland. E-mail: mda.alam@tyndall.ie, michael.nolan@tyndall.ie

†Electronic supplementary information (ESI) available: Phonon band structures of MOX$_2$ monolayers in paraelectric and ferroelectric phases, phonon band structures of the TiOF$_2$ monolayer, Young's modulus and Poisson's ratio, GGA+U$_{eff}$ calculations for e_{ij}, C_{ij}, and d_{ij}, structural and piezoelectric properties of VOCl$_2$(AFM3) and VOBr$_2$(AFM3). See DOI: https://doi.org/10.1039/d2nr02761e

cally modified graphene,[13–15] metal dichalcogenides or oxides, and Janus monolayers.[6–9,11,16–18] Encouragingly, although 2D ferroelectrics are relatively rare to date, giant in-plane piezoelectric response is present in the ferroelectric monolayers of group-IV monochalcogenides[19] and MXenes (e.g., Sc_2CS_2).[20] A huge out-of-plane piezo-response (d_{33} = 172.61 pm V^{-1}) is observed in buckled monolayers.[21] Ferroelectric In_3Se_3 nanoflakes[22] also show a moderate out-of-plane piezo-response. Furthermore, the co-existence of piezoelectricity and magnetism and their coupling in 2D materials – namely vanadium dichalcogenide monolayers,[23] Janus ferromagnetic NiClI monolayers,[11] and 1H-LaBr$_2$ monolayers[24]– have been investigated. Any strong coupling between piezoelectricity and magnetism can be utilized for making piezoelectric-based multifunctional nano-devices. In this regard, multiferroelectric materials are interesting because they usually exhibit good coupling between electric polarization and magnetic order. Piezoelectricity is linked with electric polarization – for instance, the piezoelectric stress co-efficient (e_{ij}) is defined as $\frac{\partial P_i}{\partial \eta_j}$, where strain $\partial \eta_j$ along the j-direction induces polarization along the i-direction (∂P_i). However, how changes in the magnetic order will change the piezo-response in 2D multiferroelectrics – where polarization couples with the magnetic order – remains unanswered to the best of our knowledge.

Based on first-principles calculations, several approaches such as defect engineering,[25] doping/charging,[26] and chemical functionalization[27,28] have been proposed for combining ferroelectricity and magnetism in 2D materials. There are also a limited number of intrinsically multiferroelectric 2D materials discovered recently – including the metal phosphorus chalcogenides family,[29,30] buckled CrN and CrB$_2$ monolayers,[31] and MXene Hf$_2$VC$_2$F$_2$ monolayers.[32] Multiferroelectricity in the monolayers of the metal oxyhalide VOX$_2$ family[33–37] has been predicted with interesting violation of the d^0 rule.[38] In VOX$_2$ monolayers, the ferroelectric polarization direction is perpendicular to the partially occupied d$_{xy}$ orbital that is the origin of magnetism. As a result, the partially occupied d orbital does not suppress the ferroelectric atomic displacement. Moreover, compared to ferroelectric TiOX$_2$ monolayers with the empty d orbital, the presence of an electron in the d$_{xy}$ of VOX$_2$ monolayers rather positively contributes to the total electric polarization.[34] Initially, the ground state of the VOI$_2$ monolayer was predicted as ferromagnetic and ferroelectric.[34] However, later it has been predicted that the ferroelectric VOI$_2$ monolayer can exhibit spiral magnetism for a short period due to iodine's strong (compared to other halogens) spin–orbit coupling (SOC).[36,37] Alternatively, ferroelectricity in the VOI$_2$ monolayer can also be suppressed by on-site strong Coulomb interaction making it a ferromagnetic metal.[37] The coexistence of ferroelectricity and ferromagnetism is predicted in the VOF$_2$ monolayer,[35] whereas VOCl$_2$ and VOBr$_2$ monolayers have a ferroelectric ground state with antiferromagnetic (AFM) spin order.[33,34] Note that the VOCl$_2$ monolayer can be exfoliated experimentally from its bulk layered van der Waals structure (space group: Immm).[33] Generally, ferroelectric materials exhibit good piezo-

electricity. Although ferroelectricity and multiferroelectricity of MOX$_2$ monolayers have been investigated,[33–37] their piezoelectric properties remain unknown to date. In this paper, we investigate the piezoelectric properties of both TiOX$_2$ and VOX$_2$ monolayers and how the piezo-response changes with magnetic order, which remain unexplored to date. We find that these monolayers exhibit a remarkably large piezo-response compared to most of the known 2D piezoelectrics, and they are promising materials for nanoscale electromechanical applications.

2 Computational details

Our first-principles calculations are performed in the framework of spin-polarized density functional theory as implemented in the Vienna Ab initio Simulation Package (VASP) based on a plane-wave basis set.[39] The projector augmented wave (PAW) potentials[40] are used for describing the core electrons. The generalized gradient approximation (GGA) of Perdew, Burke, and Ernzernhof (PBE)[41] is employed for treating the exchange and correlation. The valence electron configurations considered for Ti, V, O, F, Cl, and Br are 3d^3 4s^1 (4 electrons), 3d^4 4s^1 (5 electrons), 2s^2 2p^4 (6 electrons), 2s^2 2p^5 (7 electrons), 3s^2 3p^5 (7 electrons), and 4s^2 4p^5 (7 electrons), respectively. A cutoff energy of 500 eV is used for the plane-wave expansion in all calculations. All structures are fully relaxed until the Hellmann–Feynman forces on all the atoms are less than 10^{-3} eV Å^{-1}. The lattice parameters a and b are relaxed, keeping c fixed as required for 2D materials, and the internal coordinates of the 2D structures are fully relaxed to achieve the lowest energy configuration using the conjugate gradient algorithm. To prevent the interaction between the periodic images in the calculations, a vacuum layer with a thickness of approximately 25 Å is added along the z-direction (perpendicular to the monolayer) in the supercell. Note that previous reports[33–35] employed about 15–20 Å vacuum layers, and also considered the van der Waals interaction between the layers.[33,35] However, we have not considered the van der Waals interaction as we simulate an isolated monolayer. The convergence for the total energy is set as 10^{-7} eV. For a 1 × 1 × 1 unit cell, the Brillouin zone integration is sampled using a regular 12 × 12 × 1 Monkhorst–Pack k-point grid for geometry optimizations, while a denser grid of 18 × 18 × 1 is used for density functional perturbation theory (DFPT) calculations. To study magnetic ordering, 1 × 2 × 1, 2 × 1 × 1, and 2 × 2 × 1 VOX$_2$ supercells (shown in Fig. 1(c)) with 12 × 6 × 1, 6 × 12 × 1, and 6 × 6 × 1 Monkhorst–Pack k-point grids, respectively are used. The elastic stiffness coefficients (C_{ij}) are obtained using a finite difference method as implemented in the VASP code. DFPT is used to calculate the Born effective charges (Z_{ij}) and ionic and electronic parts of piezoelectric (e_{ij}) tensors. A 4 × 4 × 1 supercell is used for the phonon dispersion calculations of the monolayers, which is obtained with PHONOPY code[42] using the DFPT method. Recently it has been found that the Hubbard effective U (U_{eff}) correction does not alter the magnetic and ferroelectric properties of VOF$_2$.[35] However,
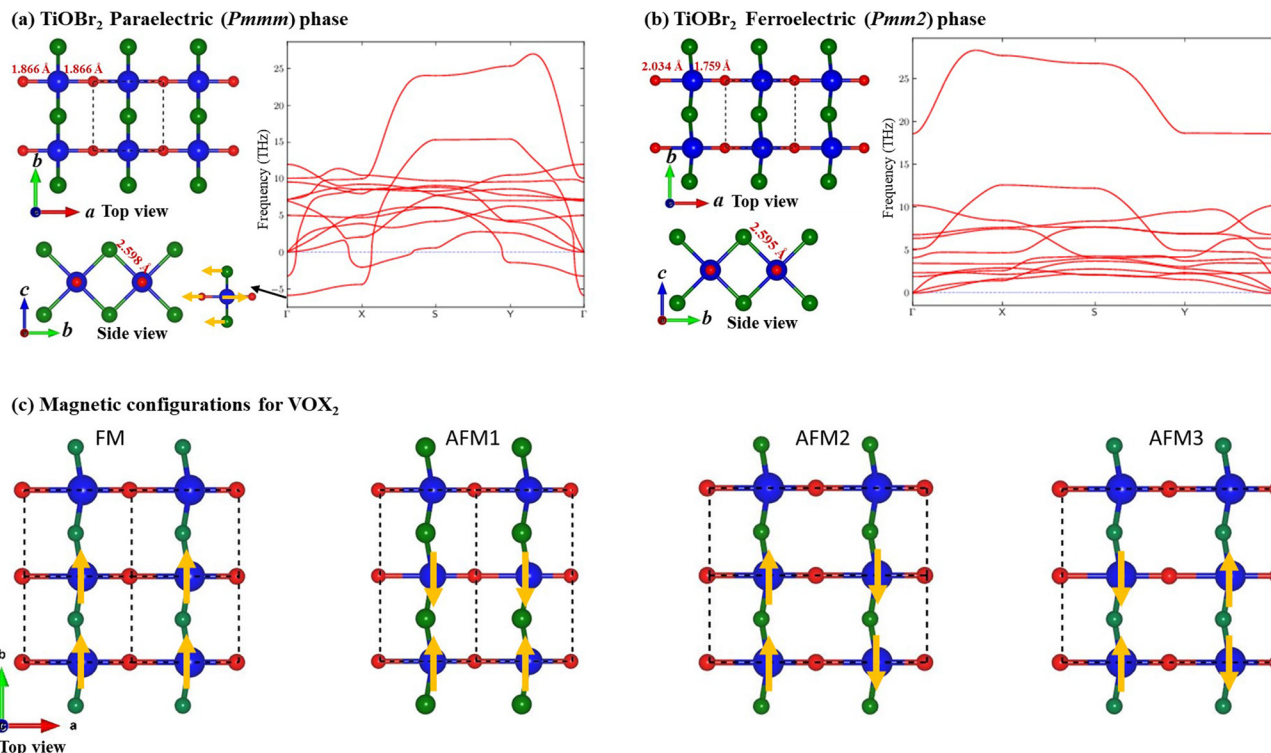
Fig. 1 As a representative of MOX_2 monolayers, top and side views of the $TiOBr_2$ monolayer in (a) the paraelectric and (b) ferroelectric phases are shown. Beside the structure, the phonon band structure is also shown. We see an imaginary phonon (soft) mode at the Γ-point for paraelectric $TiOBr_2$; the vibration mode is indicated by the black arrow, whereas yellow arrows represent the direction of atomic displacement associated with the imaginary mode. In the phonon band structure, Γ(0,0,0), X(1/2,0,0), S(1/2,1/2,0), and Y(0,1/2,0) are the high symmetric points in the Brillouin zone. Blue, red, and green balls represent Ti/V, O, and F/Cl/Br, respectively. (c) The four magnetic configurations for VOX_2 monolayers are shown; yellow arrows represent the collinear spin direction (up or down). The dashed lines represent the rectangle simulation cells.

to confirm the lack of impact of the Hubbard + U correction on the piezoelectric response of $VOBr_2$, we apply the GGA + U_{eff} (U_{eff} ranging from 1 eV to 3 eV) approach[43] for the 3d orbitals of V. We find that the Hubbard U_{eff} correction increases both e_{11} and d_{11} (see the ESI†). This further supports our conclusion that $VOBr_2$ has a large piezoelectric response.

3 Results and discussion

We start with the fully optimized centrosymmetric paraelectric (and also ferromagnetic for VOX_2) phase (space group: *Pmmm*) of MOX_2 monolayers and calculated their phonon dispersion. We find that there is an imaginary (soft) optical vibration mode at the center of the Brillouin zone (Γ-point) for the PE phase (see Fig. 1(a) for $TiOBr_2$ and also the ESI† for other MOX_2 monolayers). The frequency ($i\omega_\Gamma$) associated with the polar soft mode is given in Table 1. This suggests that there is a spontaneous atomic displacement of Ti(v) along the Ti–O (V–O) chain, breaking the inversion symmetry, thus producing a spontaneous in-plane (along the *a*-direction) electric polarization. This can also be understood in terms of long and short Ti–O (V–O) bonds along the *a*-direction in the FE phase (space group: *Pmm*2), whereas all M–O bonds are the same in the PE

phase. Therefore, the *a* lattice parameter of the FE phase becomes slightly larger than that of the PE phase, although the *b* lattice parameter remains almost unchanged (see Table 1). As Ti^{4+} and V^{4+} have almost the same ionic radii, their lattice parameters are close. We see an increase in *b* as the radius of X increases from F to Br, which is expected because X atoms are only along the *b*-direction. With the exception of $TiOF_2$ (FE), the phonon dispersion of FE MOX_2 monolayers shows no appreciable soft mode, indicating their stability. Interestingly, we find that the ground state of the $TiOF_2$ monolayer is not the FE (*Pmm*2) phase – rather the nonpolar (*Pmma*) phase (see the ESI†), which is 26.620 meV per atom lower in energy than the FE phase – therefore, we will not discuss its properties in the main paper.

As electric polarization (P_1) arises due to the polar distortion from the PE phase, we calculated P_1 in the 2D unit (C m^{-1}) using Z_{11} and the atomic displacement ($\Delta u_{k,1}$) of the *k*-th atom along the *a*-direction as $P_1 = \frac{e}{A} \sum_k \bar{Z}_{k,11} \Delta u_{k,1}$. The sum runs over all the atoms in the simulation cell; *A* is the area of the cell and *e* is charge of an electron. We use mean BECs ($\bar{Z}_{k,11}$) – *i.e.*, $\bar{Z}_{k,11} = \frac{Z_{k,11}(\text{PE}) + Z_{k,11}(\text{FE})}{2}$ because Z_{11} changes during the PE-to-FE phase transition. For the PE phase, we

Table 1 Structural information of the monolayers: optimized lattice parameters (a and b; see the rectangular cells in Fig. 1). M–O (M–X) represents the bond length between metal (M) and oxygen (halogen; X) atoms. Z_{11} is the Born effective charge in |e| unit. The values in the parentheses are for paraelectric phases. P_1 and ΔE are the in-plane electric polarization in 2D unit (C m^{-1}) and the energy difference between the ferroelectric and paraelectric phases (the positive ΔE value suggests that the FE phase is lower in energy compared to the PE phase). $i\omega_\Gamma$ stands for the lowest imaginary frequency of the PE phase at the Γ-point

	a (Å)	b (Å)	M–O (Å)	M–X (Å)	Z_{11} (M)	Z_{11} (O)	Z_{11} (X)	P_1 (10^{-12} C m^{-1})	ΔE (meV per fu)	$i\omega_\Gamma$ (cm^{-1})
VOF$_2$(FM)	3.765	3.025	1.649	1.969	5.458	−4.142	−0.659	309.192	124.809	385.919
	(3.600)	(3.055)	(1.800)	(1.971)	(13.235)	(−10.188)	(−1.415)			
VOCl$_2$(FM)	3.773	3.454	1.653	2.388	4.893	−4.255	−0.319	288.284	119.122	351.430
	(3.610)	(3.480)	(1.805)	(2.397)	(14.703)	(−12.174)	(−1.197)			
VOCl$_2$(AFM1)	3.784	3.367	1.650	2.383	4.825	−4.186	−0.319	311.609	129.095	396.542
	(3.609)	(3.408)	(1.804)	(2.395)	(15.171)	(−12.926)	(−1.122)			
VOBr$_2$(FM)	3.764	3.649	1.664	2.545	5.018	−4.579	−0.219	254.575	82.916	285.802
	(3.620)	(3.620)	(1.810)	(2.557)	(15.076)	(−12.965)	(−1.029)			
VOBr$_2$(AFM1)	3.769	3.577	1.661	2.542	5.025	−4.580	−0.222	271.205	85.646	301.611
	(3.619)	(3.615)	(1.810)	(2.555)	(14.931)	(−13.065)	(−0.933)			
TiOCl$_2$	3.793	3.504	1.745	2.438	7.506	−6.723	−0.391	185.430	26.519	227.851
	(3.719)	(3.518)	(1.859)	(2.441)	(12.291)	(−11.011)	(−0.391)			
TiOBr$_2$	3.792	3.677	1.759	2.595	7.931	−7.347	−0.289	160.291	16.254	170.826
	(3.732)	(3.689)	(1.866)	(2.598)	(11.973)	(−11.012)	(−0.480)			

find anomalously large Z_{11}, which decreases after the PE-to-FE transition (see Table 1). Similar anomalous BECs have been observed for other well-known ferroelectric materials.[44] In agreement with previous reports,[35] we find that MOX$_2$ monolayers have quite large P_1, which is comparable with that of group-IV monochalcogenide orthorhombic monolayers, e.g., SnS ($P_1 = 2.47 \times 10^{-10}$ C m^{-1}).[45,46] We also estimated the energy barrier for FE polarization switching. We take the difference in energy (ΔE) between FE and PE phases; lattice parameters a and b are fully relaxed in both phases. Our ΔE values are in good agreement with the reported values. We see a general trend that P_1, ΔE, and $i\omega_\Gamma$ decrease as the ionic radius of X increases from F to Br. Interestingly, we also observed that magnetic VOX$_2$ monolayers have significantly larger P_1 than non-magnetic TiOCl$_2$ or TiOBr$_2$. This is in line with the previous report that the presence of an electron in the d$_{xy}$ orbital of V does not suppress but rather enhances ferroelectric polarization.[34] This is also confirmed by the larger $i\omega_\Gamma$ of VOX$_2$ (see Table 1).

To examine the impact of magnetic configuration on VOX$_2$ monolayers, we consider four (1 FM and 3 AFM) collinear magnetic spin configurations (see Fig. 1(c) and Table 2). Each V^{4+} contributes $1\mu_B$, which comes from an unpaired electron in the d$_{xy}$ orbital.[34] Comparing the energy difference of an AFM configuration with respect to the FM order, in agreement with previous reports, we find that the FE VOF$_2$ monolayer has an

FM ground state.[35] However, we find that the AFM3-type AFM order (see Fig. 1(c)) is more stable than other configurations in VOCl$_2$ and VOBr$_2$ monolayers.[33,34] The alternating up and down collinear spin configuration of V atoms along the b-direction (see Fig. 1(c)) shortens the b lattice parameter, compared with that of the FM state (shown in Table 1). By applying an external magnetic field in an experiment, the AFM order can be changed to FM. This will also lead a change in P_1 with a reduction of 7.49% and 6.13% for AFM1-to-FM transition in VOCl$_2$ and VOBr$_2$ monolayers, respectively. The AFM1-to-FM transition slightly hardens the soft mode ($i\omega_\Gamma$; see Table 1; also see the ESI† for AFM3), and consequently reduces the ferroelectric switching barrier (ΔE) slightly. This indicates that there is a weak coupling between the magnetic and ferroelectric orders in VOX$_2$.

All ferroelectrics exhibit piezoelectricity. It is interesting to know the piezo-response of our FE MOX$_2$ monolayers as strong in-plane piezoelectricity has already been predicted in 2D FE group-IV monochalcogenides.[19] Our calculated piezoelectric stress coefficients (e_{ij}) are shown in Table 3. e_{ij} are important coefficients for estimating the figure-of-merit of a piezoelectric thin-film (TFFOM); usually the larger the e_{ij}, the higher the figure-of-merit. Because strain along the z-direction (vacuum) is ill-defined in 2D materials, we have only three independent piezoelectric coefficients: e_{11}, e_{12}, and e_{16}. There is a mirror symmetry along the b-direction, which does not allow any polarization in that direction, thus $e_{22} = 0$. However, strain along the b-direction can induce polarization along the a-direction, which results in a non-zero e_{12} coefficient. The FE MOX$_2$ monolayer (space group: $Pmm2$) due to the $mm2$ point group has a symmetry of reflection with reference to the M–O atomic plane. This prohibits an out-of-plane electric polarization, thus $e_{31} = 0$. We mainly focus on the piezo-response related to uniaxial strain along the a-direction (η_1) and the b-direction (η_2), which are $e_{11}(d_{11})$ and $e_{12}(d_{12})$, respectively. e_{16} is associated with shear strain (η_{12}),[19] and we exclude it for simplicity.

Table 2 Energy difference ($\Delta E_{AFM} = E_{AFM} - E_{FM}$; E_{AFM} and E_{FM} are the energy per unit-formula of fully-relaxed structures in AFM and FM magnetic orders, respectively) in meV per unit formula of 3 magnetic configurations with respect to the FM order; negative means the AFM configuration is more stable than the FM order

	ΔE_{AFM1}	ΔE_{AFM2}	ΔE_{AFM3}
VOF$_2$	9.183	2.170	9.789
VOCl$_2$	−20.331	3.652	−22.019
VOBr$_2$	−9.437	4.774	−11.257

Table 3 The electronic (e_{11}^{elc} and e_{12}^{elc}) and ionic (e_{11}^{ion} and e_{12}^{ion}) parts of the total piezoelectric stress constants e_{11} and e_{12} in the 2D piezoelectric unit of 10^{-10} C m^{-1} of the MOX$_2$ monolayers, and the Born effective charges (Z_{11}) of metals (Ti and V), O, and halogens (X = F, Cl, and Br) in the charge of an electron (|e|) unit. $\frac{du_1}{d\eta_1}$ or $\frac{du_1}{d\eta_2}$ represents the change of the atomic coordinates along the a-direction in response to a strain along the a-direction (η_1) or the b-direction (η_2), respectively

	e_{11}^{elc}	e_{11}^{ion}	e_{11}	$\frac{du_1(M)}{d\eta_1}$	$\frac{du_1(O)}{d\eta_1}$	$\frac{du_1(X)}{d\eta_1}$	e_{12}^{elc}	e_{12}^{ion}	e_{12}	$\frac{du_1(M)}{d\eta_2}$	$\frac{du_1(O)}{d\eta_2}$	$\frac{du_1(X)}{d\eta_2}$
VOF$_2$(FM)	5.776	13.850	19.625	0.271	−0.242	−0.015	4.513	−0.867	3.646	−0.073	−0.060	0.066
VOCl$_2$(FM)	4.524	11.397	15.921	0.315	−0.213	−0.051	3.354	−0.639	2.716	−0.044	−0.037	0.041
VOCl$_2$(AFM1)	4.693	11.407	16.100	0.314	−0.209	−0.052	3.309	−0.693	2.616	−0.029	−0.021	0.025
VOBr$_2$(FM)	4.217	11.937	16.153	0.371	−0.195	−0.088	2.974	−0.824	2.150	−0.039	−0.031	0.035
VOBr$_2$(AFM1)	4.331	12.384	16.715	0.371	−0.191	−0.090	2.962	−0.437	2.526	−0.029	−0.022	0.025
TiOCl$_2$	3.764	22.345	26.109	0.494	−0.177	−0.159	1.819	−1.103	0.716	−0.038	−0.028	0.033
TiOBr$_2$	3.250	25.543	28.793	0.599	−0.162	−0.218	1.531	−0.737	0.794	−0.034	−0.024	0.029

Table 3 shows that the TiOCl$_2$ or TiOBr$_2$ monolayer has quite large e_{11} but small e_{12}, compared to those of VOX$_2$ monolayers. We also notice that unlike 1H-type monolayers, e.g., 1H-MoS$_2$ where $e_{11} = -e_{12}$ due to the $\bar{6}m2$ point group symmetry, MOX$_2$ monolayers exhibit a highly anisotropic piezoresponse, where e_{11} is significantly larger than e_{12}. This is also expected as the monolayers have a strong in-plane electric polarization P_1, hence atomic displacement in response to strain along the a-direction can change P_1 directly. Interestingly, we observe a general trend that the in-plane piezo-response (e_{11}) decreases as the in-plane polarization increases (see Tables 1 and 3). To understand the origin of the large/small piezoelectric constant, we split e_{11} and e_{12} into two terms – (i) the clamped-ion term (e_{11}^{elc} or e_{12}^{elc}), which is the electronic contribution where the atoms are fixed at their equilibrium internal coordinates (u) and (ii) the ionic contribution term (e_{11}^{ion} or e_{12}^{ion}), due to the atomic displacements in response to a macroscopic strain η_1 (η_2) along the a-direction (b-direction). The e_{11}^{ion} of TiOCl$_2$ and TiOBr$_2$ monolayers is almost twice larger than that of VOX$_2$. Interestingly, we notice that both ionic and electronic parts of e_{11} are positive (see Table 3), thus they contribute positively to the total e_{11} – similar to 1H-MoS$_2$.[24] That is why the TiOCl$_2$ or TiOBr$_2$ monolayer has significantly large e_{11}, compared to that of VOX$_2$, although the e_{11}^{elc} of TiOCl$_2$ and TiOBr$_2$ monolayers is slightly smaller than that of VOX$_2$. On the other hand, the ionic and electronic parts of e_{12} are opposite in sign, hence they reduce the total e_{12}. We see that because of their small positive e_{12}^{elc} but large negative e_{12}^{ion}, TiOCl$_2$ and TiOBr$_2$ monolayers have quite small e_{12} (see Table 3). We further split the ionic part:[24,47,48]

$$e_{11}^{\text{ion}} = \sum_k e_{11}^{\text{ion}}(k) = \sum_k \frac{ea}{A} Z_{11}(k) \frac{du_1(k)}{d\eta_1} \quad (1)$$

$$e_{12}^{\text{ion}} = \sum_k e_{12}^{\text{ion}}(k) = \sum_k \frac{ea}{A} Z_{11}(k) \frac{du_1(k)}{d\eta_2} \quad (2)$$

e_{11}^{ion} or e_{12}^{ion} involves summation running over all the atoms (k) in a cell, e is the charge of an electron, and A is the area of the cell of the 2D unit. The response of the k-th atom's internal coordinate along the a-direction ($u_1(k)$) in response to a macro-

scopic strain (η_1) in the same direction is measured by $\frac{du_1(k)}{d\eta_1}$. Similarly, $\frac{du_1(k)}{d\eta_2}$ represents the change in the k-th atom's internal coordinate along the a-direction ($u_1(k)$) in response to a macroscopic strain (η_2) along the b-direction. Relaxing the atomic positions in response to the strains η_1 and η_2, we obtain the slopes $\frac{du_1(k)}{d\eta_1}$ and $\frac{du_1(k)}{d\eta_2}$, respectively. We notice that the large e_{11}^{ion} of TiOCl$_2$ and TiOBr$_2$ monolayers comes from their large Z_{11} (see Table 1) and $\frac{du_1}{d\eta_1}$ (see Table 3). Also, we see that the $\frac{du_1}{d\eta_1}$ of Ti/V/O is an order of magnitude larger than $\frac{du_1}{d\eta_2}$ – i.e., the uniaxial strain η_1 can displace atoms along the a-direction more than η_2. This also gives the large difference between e_{11}^{ion} and e_{12}^{ion}. Moreover, we observe that the AFM1 order of VOCl$_2$ and VOBr$_2$ marginally enhances e_{11} because of a slight increase in both e_{11}^{elc} and e_{11}^{ion} (see Table 3). Note that a change in the magnetic order also changes the e_{ij} of other magnetic 2D piezoelectrics.[24] Piezoelectric constants for AFM3 of VOCl$_2$ and VOBr$_2$ are presented in the ESI†.

Note that the e_{11} of MOX$_2$ monolayers is significantly (about 6–10 times) larger than that of the well-known 1H-type piezoelectric monolayers e.g., 1H-MoS$_2$ ($e_{11} = 3.64 \times 10^{-10}$ C m^{-1}).[4,6,8] We notice that the e_{11}^{ion} of MOX$_2$ monolayers is an order of magnitude larger than that of 1H-MoS$_2$ or 1H-VS$_2$,[24] although their electronic parts are quite comparable.[24] Both the Z_{11} and $\frac{du_1}{d\eta_1}$ of MOX$_2$ monolayers are remarkably higher than those of 1H-MoS$_2$ or 1H-VS$_2$.[24] Our e_{11} is quite comparable with that of group-IV monochalcogenide monolayers such as SnS,[19] although the difference between e_{11} and e_{12} in group-IV monochalcogenides is not as pronounced as in MOX$_2$ monolayers. Note that the large piezo-response of our MOX$_2$ is very similar to that of ferroelectric niobium oxyhalide monolayers.[49]

For piezoelectric thin-film-based applications, $\frac{e_{11}^2}{\varepsilon_0 \varepsilon_{11}}$, where ε_0 and ε_{11} are the vacuum permittivity and static dielectric constant, respectively, is a key figure-of-merit (TFFOM).[49] A recent high-throughput calculation has found that niobium oxyhalide

Table 4 Elastic constants (C_{11}, C_{22}, C_{12}, and C_{66}) in the 2D unit of N m^{-1} and the piezoelectric strain coefficient in d_{11} and d_{12} in pm V^{-1}. *VOCl$_2$(FM) and *VOBr$_2$ (FM) represent the structures with the FM order but their lattice parameters and atomic positions are fixed at those of their AFM1 configurations

	C_{11}	C_{22}	C_{12}	C_{66}	d_{11}	d_{12}
VOF$_2$(FM)	67.999	96.795	15.073	22.404	29.028	−0.753
VOCl$_2$(FM)	53.761	58.255	8.711	18.808	29.575	0.239
VOCl$_2$(AFM1)	50.810	42.460	6.887	18.640	31.545	1.045
*VOCl$_2$(FM)	49.929	58.242	6.381	18.557	31.288	0.874
VOBr$_2$(FM)	54.694	50.240	7.528	17.176	29.555	−0.149
VOBr$_2$(AFM1)	52.998	40.485	6.196	17.132	31.372	1.437
*VOBr$_2$(FM)	53.134	51.124	5.935	17.021	30.779	2.054
TiOCl$_2$	78.264	56.536	8.318	16.971	33.753	−3.700
TiOBr$_2$	76.942	47.862	6.879	15.029	37.758	−3.768

monolayers have a significantly large TFFOM (in the range of 59.60 nN–71.70 nN) compared to other 2D piezoelectrics (e.g., the TFFOM of CuInP$_2$Se$_6$ is 3.10 nN).[49] We find that the TFFOM of MOX$_2$ monolayers is remarkably higher than that of niobium oxyhalide monolayers,[49] in the range of 105.43 nN for VOBr$_2$–203.43 nN for TiOBr$_2$, indicating their potential for flexible piezoelectric nano-devices. The TFFOMs of TiOCl$_2$, VOF$_2$, and VOCl$_2$ are 201.57 nN, 187.57 nN, and 118.47 nN, respectively, which are huge compared to the TFFOM of 1H-MoS$_2$ (3.45 nN; note that our calculated ε_{11} of 1H-MoS$_2$ is 4.51, which is consistent with the previous report of 4.20[50]). Such high TFFOMs of MOX$_2$ monolayers are the result of their low dielectric constants (ε_{11}) and large e_{11} values. The ε_{11} values of TiOCl$_2$, TiOBr$_2$, VOF$_2$, VOCl$_2$, and VOBr$_2$ are 3.82, 4.60, 2.32, 2.42, and 2.80, respectively, whereas the ε_{11} values of niobium oxyhalide monolayers are in the range of 12–15.[49]

Our piezoelectric strain constants (d_{ij}) – another important figure of merit for many piezoelectric applications – are obtained using e_{ij} and elastic constants (C_{ij}) (see Table 4): $d_{11} = \dfrac{C_{22}e_{11} - C_{12}e_{12}}{C_{11}C_{22} - C_{12}^2}$ and $d_{12} = \dfrac{C_{11}e_{12} - C_{12}e_{11}}{C_{11}C_{22} - C_{12}^2}$. The nonzero and independent C_{ij} in the Voigt notation of FE MOX$_2$ monolayers are given in Table 4, and they also are positive (i.e., C_{11}, C_{22}, C_{12}, and $C_{66} > 0$), indicating their mechanical stability; our orthorhombic monolayers clearly satisfy the Born elastic stability criterion:[51] $C_{11}C_{22} - C_{12}^2 > 0$. Unlike 1H-type monolayers, MOX$_2$ are anisotropic elastically (i.e., $C_{11} \neq C_{22}$ – Young's modulus (Y) and Poisson's ratio (ν) along the a-direction are also different from those along the b-direction; these are presented in the ESI.† Note that Y quantifies how easily a material can be stretched and deformed, whereas ν quantifies the deformation in the material in a direction perpendicular to the applied force's direction). We find large d_{11} for MOX$_2$ monolayers – and small d_{12}. However, the d_{12} of TiOCl$_2$ or TiOBr$_2$ is quite comparable with that of 1H-MoS$_2$ (3.73 pm V^{-1})[4] or 1H-VS$_2$ (4.104 pm V^{-1}).[24] TiOBr$_2$ has the largest d_{11} (37.758 pm V^{-1}), which is 2–10 times larger than those of 1H-type monolayers[4,6,8] (e.g., d_{11} of 1H-MoS$_2$ and 1H-CrTe$_2$ is 3.65 pm V^{-1} and 13.45 pm V^{-1}, respectively[6]). This is because compared to 1H-type piezoelectrics, MOX$_2$ have significantly larger e_{11} and relatively smaller elastic constants (e.g., the C_{11} of 1H-MoS$_2$ is 130 N m^{-1}[4]). Note that the d_{11} of MOX$_2$ is very

similar to that of niobium oxyhalide monolayers (27.4 pm V^{-1} to 42.20 pm V^{-1}).[49] Interestingly, in comparison to bulk piezoelectric materials, we find that the piezo-response of MOX$_2$ monolayers is remarkably strong. For example, the d_{11} (37.758 pm V^{-1}) of TiOBr$_2$ is an order of magnitude larger than that of α-quartz ($d_{11} = 2.3$ pmV^{-1})[52] or the d_{33} of w-GaN (3.1 pm V^{-1});[53] and also about 7 times higher than the d_{33} of w-AlN (5.1 pm V^{-1}).[53] Note that group-IV monochalcogenide monolayers[19] have relatively smaller – indicating their softness – C_{11} and C_{22} (e.g., $C_{11} = 20.87$ N m^{-1} and $C_{22} = 53.40$ N m^{-1} for GeS monolayer[19]) than MOX$_2$ monolayers. That is why group-IV monochalcogenide monolayers have larger d_{11} (e.g., $d_{11} = 75.43$ pm V^{-1} of the GeS monolayer)[19] than that of MOX$_2$.

As VOCl$_2$ and VOBr$_2$ monolayers have an AFM ground state, we also study how their piezo-response will change in response to the AFM-to-FM phase transition, which can be experimentally possible under an external magnetic field.[54] Note that the FM-to-AFM transition can be a challenge in experiments. We find that the AFM1-to-FM transition somewhat increases the elastic constants – especially C_{22} – thus slightly decreases d_{11}. Interestingly, such hardening of C_{22} is intrinsic to the AFM1-to-FM transition as we see that it comes from the mere magnetic order change even if the lattice parameters and atomic positions are fixed at AFM1 (see Table 4). There is a significant decrease in d_{12} (see Table 4). Interestingly, d_{12} changes its sign during the AFM1-to-FM transition for the VOBr$_2$ monolayer, indicating that subject to an external electric field the monolayer can shrink or expand depending on the presence of a magnetic field. This can allow us to control piezoelectricity by magnetism, which may find applications in realizing multifunctional nano-devices. We believe that other magnetic piezoelectrics, especially 2D multiferroelectric, can also exhibit such coupling between piezo-response and magnetic order.

4 Conclusion

Our first principles calculations demonstrate that FE MOX$_2$ monolayers have a strong in-plane piezoelectric response, which is not only significantly larger than that of the well-known 1H-type 2D piezoelectrics – e.g., both the e_{11} and d_{11} of

MOX_2 are about an order of magnitude larger than those of $1H\text{-}MoS_2$ – but also remarkably stronger than some of bulk piezoelectrics such as w-AlN or w-GaN. These monolayers also exhibit a remarkably large anisotropy in their piezo-response – *i.e.*, piezo-response due to strain along the *a*-direction is about an order of magnitude larger than that of along the *b*-direction. We also show that a change in the magnetic order can change the piezo-response in multiferroelectric VOX_2 monolayers, which can potentially couple piezoelectricity and magnetism. We believe that this work will inspire more research in searching for new piezoelectric materials that can couple strongly with magnetism. Also, such a large in-plane piezo-response can particularly be beneficial for 2D nanoscale flexible piezo-devices – *e.g.*, actuators purely based on in-plane displacement.

Conflicts of interest

There are no conflicts to declare.

Acknowledgements

References

1 Q. Zhang, S. Zuo, P. Chen and C. Pan, *InfoMat*, 2021, **3**, 987–1007.
2 Y. Liu, E. T. N. Wahyudin, J.-H. He and J. Zhai, *MRS Bull.*, 2018, **43**, 959–964.
3 G. Michael, Y. Zhang, J. Nie, D. Zheng, G. Hu, R. Liu, M. Dan, L. Li and Y. Zhang, *Nano Energy*, 2020, **76**, 105091.
4 K.-A. N. Duerloo, M. T. Ong and E. J. Reed, *J. Phys. Chem. Lett.*, 2012, **3**, 2871–2876.
5 H. Zhu, Y. Wang, J. Xiao, M. Liu, S. Xiong, Z. J. Wong, Z. Ye, Y. Ye, X. Yin and X. Zhang, *Nat. Nanotechnol.*, 2015, **10**, 151–155.
6 M. N. Blonsky, H. L. Zhuang, A. K. Singh and R. G. Hennig, *ACS Nano*, 2015, **9**, 9885–9891.
7 K. H. Michel, D. Çakir, C. Sevik and F. M. Peeters, *Phys. Rev. B*, 2017, **95**, 125415.
8 M. M. Alyoruk, Y. Aierken, D. Çakir, F. M. Peeters and C. Sevik, *J. Phys. Chem. C*, 2015, **119**, 23231–23237.
9 Y. Lu and S. B. Sinnott, *ACS Appl. Nano Mater.*, 2020, **3**, 384–390.
10 P. Nandi, A. Rawat, R. Ahammed, N. Jena and A. De Sarkar, *Nanoscale*, 2021, **13**, 5460–5478.
11 S.-D. Guo, Y.-T. Zhu, K. Qin and Y.-S. Ang, *Appl. Phys. Lett.*, 2022, **120**, 232403.
12 Z. Kahraman, A. Kandemir, M. Yagmurcukardes and H. Sahin, *J. Phys. Chem. C*, 2019, **123**, 4549–4557.
13 M. T. Ong and E. J. Reed, *ACS Nano*, 2012, **6**, 1387–1394.
14 M. T. Ong, K.-A. N. Duerloo and E. J. Reed, *J. Phys. Chem. C*, 2013, **117**, 3615–3620.
15 H. J. Kim, M. Noor-A-Alam and Y.-H. Shin, *J. Appl. Phys.*, 2015, **117**, 145304.
16 M. Noor-A-Alam, H. J. Kim and Y.-H. Shin, *J. Appl. Phys.*, 2015, **117**, 224304.
17 M. Noor-A-Alam, H. J. Kim and Y.-H. Shin, *Phys. Chem. Chem. Phys.*, 2014, **16**, 6575–6582.
18 R. Ahammed, N. Jena, A. Rawat, M. K. Mohanta, Dimple and A. De Sarkar, *J. Phys. Chem. C*, 2020, **124**, 21250–21260.
19 R. Fei, W. Li, J. Li and L. Yang, *Appl. Phys. Lett.*, 2015, **107**, 173104.
20 L. Zhang, C. Tang, C. Zhang and A. Du, *Nanoscale*, 2020, **12**, 21291–21298.
21 M. K. Mohanta, F. IS, A. Kishore and A. De Sarkar, *ACS Appl. Mater. Interfaces*, 2021, **13**, 40872–40879.
22 Y. Zhou, D. Wu, Y. Zhu, Y. Cho, Q. He, X. Yang, K. Herrera, Z. Chu, Y. Han, M. C. Downer, H. Peng and K. Lai, *Nano Lett.*, 2017, **17**, 5508–5513.
23 J. Yang, A. Wang, S. Zhang, J. Liu, Z. Zhong and L. Chen, *Phys. Chem. Chem. Phys.*, 2019, **21**, 132–136.
24 M. Noor-A-Alam and M. Nolan, *ACS Appl. Electron. Mater.*, 2022, **4**, 850–855.
25 Y. Zhao, L. Lin, Q. Zhou, Y. Li, S. Yuan, Q. Chen, S. Dong and J. Wang, *Nano Lett.*, 2018, **18**, 2943–2949.
26 C. Huang, Y. Du, H. Wu, H. Xiang, K. Deng and E. Kan, *Phys. Rev. Lett.*, 2018, **120**, 147601.
27 Q. Yang, W. Xiong, L. Zhu, G. Gao and M. Wu, *J. Am. Chem. Soc.*, 2017, **139**, 11506–11512.
28 Z. Tu, M. Wu and X. C. Zeng, *J. Phys. Chem. Lett.*, 2017, **8**, 1973–1978.
29 J. Qi, H. Wang, X. Chen and X. Qian, *Appl. Phys. Lett.*, 2018, **113**, 043102.
30 X. Feng, J. Liu, X. Ma and M. Zhao, *Phys. Chem. Chem. Phys.*, 2020, **22**, 7489–7496.
31 W. Luo, K. Xu and H. Xiang, *Phys. Rev. B*, 2017, **96**, 235415.
32 J.-J. Zhang, L. Lin, Y. Zhang, M. Wu, B. I. Yakobson and S. Dong, *J. Am. Chem. Soc.*, 2018, **140**, 9768–9773.
33 H. Ai, X. Song, S. Qi, W. Li and M. Zhao, *Nanoscale*, 2019, **11**, 1103–1110.
34 H. Tan, M. Li, H. Liu, Z. Liu, Y. Li and W. Duan, *Phys. Rev. B*, 2019, **99**, 195434.
35 H.-P. You, N. Ding, J. Chen and S. Dong, *Phys. Chem. Chem. Phys.*, 2020, **22**, 24109–24115.
36 C. Xu, P. Chen, H. Tan, Y. Yang, H. Xiang and L. Bellaiche, *Phys. Rev. Lett.*, 2020, **125**, 037203.
37 N. Ding, J. Chen, S. Dong and A. Stroppa, *Phys. Rev. B*, 2020, **102**, 165129.
38 N. A. Hill, *J. Phys. Chem. B*, 2000, **104**, 6694–6709.
39 G. Kresse and J. Furthmüller, *Phys. Rev. B: Condens. Matter Mater. Phys.*, 1996, **54**, 11169.

40 G. Kresse and D. Joubert, *Phys. Rev. B: Condens. Matter Mater. Phys.*, 1999, **59**, 1758.

41 J. P. Perdew, K. Burke and M. Ernzerhof, *Phys. Rev. Lett.*, 1996, **77**, 3865.

42 A. Togo and I. Tanaka, *Scr. Mater.*, 2015, **108**, 1–5.

43 S. L. Dudarev, G. A. Botton, S. Y. Savrasov, C. J. Humphreys and A. P. Sutton, *Phys. Rev. B: Condens. Matter Mater. Phys.*, 1998, **57**, 1505–1509.

44 P. Ghosez, J.-P. Michenaud and X. Gonze, *Phys. Rev. B: Condens. Matter Mater. Phys.*, 1998, **58**, 6224–6240.

45 M. Wu and X. C. Zeng, *Nano Lett.*, 2016, **16**, 3236–3241.

46 H. Wang and X. Qian, *2D Mater.*, 2017, **4**, 015042.

47 M. Noor-A-Alam, O. Z. Olszewski and M. Nolan, *ACS Appl. Mater. Interfaces*, 2019, **11**, 20482–20490.

48 F. Bernardini, V. Fiorentini and D. Vanderbilt, *Phys. Rev. B: Condens. Matter Mater. Phys.*, 1997, **56**, R10024–R10027.

49 Y. Wu, I. Abdelwahab, K. C. Kwon, I. Verzhbitskiy, L. Wang, W. H. Liew, K. Yao, G. Eda, K. P. Loh, L. Shen and S. Y. Quek, *Nat. Commun.*, 2022, **13**, 1884.

50 T. Cheiwchanchamnangij and W. R. L. Lambrecht, *Phys. Rev. B: Condens. Matter Mater. Phys.*, 2012, **85**, 205302.

51 F. Mouhat and F.-X. Coudert, *Phys. Rev. B: Condens. Matter Mater. Phys.*, 2014, **90**, 224104.

52 R. Bechmann, *Phys. Rev.*, 1958, **110**, 1060–1061.

53 C. M. Lueng, H. L. W. Chan, C. Surya and C. L. Choy, *J. Appl. Phys.*, 2000, **88**, 5360–5363.

54 L. V. B. Diop, T. Faske, O. Isnard and W. Donner, *Phys. Rev. Mater.*, 2021, **5**, 104401.